frontiers | Frontiers in Marine Science

TYPE Original Research
PUBLISHED 06 December 2024
DOI 10.3389/fmars.2024.1503177

OPEN ACCESS

EDITED BY
Qingjun Song,
Ministry of Natural Resources, China

REVIEWED BY
Deyong Sun,
Nanjing University of Information Science and Technology, China
Liqiao Tian,
Wuhan University, China
Tingwei Cui,
Sun Yat-sen University, China

*CORRESPONDENCE
Fei Xiao
xiaof@whigg.ac.cn

RECEIVED 28 September 2024
ACCEPTED 22 November 2024
PUBLISHED 06 December 2024

CITATION
Cao S, Xiao F, Chen M, Wang Z, Luo J and Du Y (2024) Inversion and analysis of transparency changes in the eastern coastal waters of China from 2003 to 2023 by an improved QAA-based method.
Front. Mar. Sci. 11:1503177.
doi: 10.3389/fmars.2024.1503177

Inversion and analysis of transparency changes in the eastern coastal waters of China from 2003 to 2023 by an improved QAA-based method

Shuhui Cao[1,2], Fei Xiao[1]*, Miaomiao Chen[1,2], Zhou Wang[1,2], Jiahuan Luo[1,2] and Yun Du[1]

[1]Key Laboratory for Environment and Disaster Monitoring and Evaluation of Hubei, Innovation Academy for Precision Measurement Science and Technology, Chinese Academy of Sciences, Wuhan, China, [2]University of Chinese Academy of Sciences, Beijing, China

Transparency (Z_{sd}) can most intuitively reflect changes in marine ecosystems, therefore; the data of Z_{sd} is crucial to protect marine ecosystems. However, there is still a relative lack of long-term sequence data on Z_{sd} for coastal turbid waters. Satellite remote sensing inversion provides an efficient means of obtaining long-term, large-scale Z_{sd}. The method proposed by Lee et al. is currently one of the most widely used methods, which is divided into clear water and turbid water models based on the 670 nm remote sensing reflectance (R_{rs}). In this study, we employed an improved model building upon the aforementioned method. The improved model simulates the continuous transition from clear to turbid water, which allows for automatic adjustment of model weights based on a logistic curve. Utilizing this improved model, this study inverts Z_{sd} within 100 km of the eastern coast of China from 2003 to 2023 using MODIS Aqua Level 2 R_{rs} data. Z_{sd} shows an increasing trend with the distance from the coast, with high Z_{sd} in the northern Yellow Sea, the southern Shandong Peninsula, and the far shore of the East China Sea, and the low Z_{sd} in the coast of Bohai Sea and northern Jiangsu. As for the long-term changes, the number of pixels with significantly increased Z_{sd} and those with significantly decreased Z_{sd} and no significant changes accounted for 20.84%, 1.14%, and 78.02%, respectively. The order of seasonal Z_{sd} is summer > autumn > spring > winter, and the seasonal variability amplitude increases synchronously with the offshore distance of seawater on the whole. Interestingly, the correlation between Z_{sd} and the annual runoff of rivers exhibits spatial differentiation among six typical estuaries: there are positive correlations in northern, whereas negative correlations in the south. Additionally, the Z_{sd} in five of six estuaries have negative correlations with annual sediment transport. Overall, this study not only provides more accurate and continuous data of Z_{sd} for nearshore turbid waters compared to those obtained by the original model, but also offers valuable insights on the spatiotemporal variation in the Z_{sd} of large-scale seawater.

KEYWORDS

transparency, remote sensing, coastal waters, inversion, spatiotemporal variability

1 Introduction

Global climate change and human activities have increasingly threatened the security of marine ecosystems, particularly in the coastal regions (Cael et al., 2023; Dai et al., 2023). The Bohai Sea (BS), Yellow Sea (YS), and East China Sea (ECS), situated along the edge of the northwest Pacific Ocean, face intensified environmental pressures due to pollutant and sediment inputs from major rivers in China (Shi and Wang, 2012). Although the stricter environmental protection regulations have been executed in recent years, uncertainties remain regarding the response and long-term ecological trends of marine ecosystems (Wang et al., 2023b). Fortunately, transparency, as a critical indicator of water quality, effectively indicates changes in marine environments. Thus, research on nearshore water transparency is crucial for evaluating marine ecosystem health and developing effective marine protection regulations (Basset et al., 2001; Melo et al., 2009). At present, transparency can be measured by the Secchi disk depth (Z_{sd}). This method requires consumption of massive time and resources although it can obtain accurate results, which makes it difficult for us to obtain long-term and large-scale data (Lee et al., 2016; Qing et al., 2021). In contrast, remote sensing technology has the advantages of wide monitoring area and fast data collection, which can facilitate convenient services for long-term and large-scale transparency data (Guo et al., 2022; Molner et al., 2023; Guo et al., 2023b). Over the past four decades, satellite remote sensing has been demonstrated to be an effective means of monitoring global and regional water environments (Feng et al., 2019; Jiang et al., 2019). Also, remote sensing has been successfully applied to the prediction of water Z_{sd} (Feng et al., 2019; Guo et al., 2022).

In general, the commonly used methods for retrieving Z_{sd} in remote sensing data include empirical algorithms and semi-analytical algorithms (Jiang et al., 2019). The former estimates Z_{sd} using a simple regression analysis between remote sensing data and *in-situ* measurements of Z_{sd}. This approach offers several advantages, including simplicity, convenience, and high accuracy. However, it is susceptible to limitations due to regional and temporal constraints. Differently, the latter is based on underwater visibility theory for Z_{sd} inversion (Msusa et al., 2022), which is a more commonly used method (Zhao et al., 2022). However, most of these algorithms have been designed for the ocean and do not consider the local characteristics of the ocean (He et al., 2004; Lee et al., 2015; Mao et al., 2018). For example, the semi-analytic algorithm (QAA) developed by Lee et al., and it is currently one of the most commonly used mechanism models (Lee et al., 2015). This model can derive the total absorption coefficient ($a(\lambda)$, m^{-1}) and the total backscattering coefficient ($b_b(\lambda)$, m^{-1}) from the remote sensing reflectance ($R_{rs}(\lambda)$, sr^{-1}). Based on this, the minimum diffusion attenuation coefficient ($K_d(\lambda)$, m^{-1}) within 400 - 700 nm can be calculated to ultimately determine Z_{sd}. Following the naming convention proposed by Xiang et al., we refer to the algorithm developed by Lee et al. in 2015 as "Lee15" in this study (Xiang et al., 2023). The Lee15 divided the model into clear water (QAA_{clear}) and turbid water (QAA_{turbid}) models based on the value of $R_{rs}(670)$. This method is well applied in clear water, but may generate inaccurate results when applied to highly turbid water (Lee et al., 2015; Yin et al., 2021). In fact, the ocean is usually divided into Class I water bodies (ocean) and Class II water bodies (heavily influenced by humans) (Gordon and Morel, 1983). This results in a limited practical application scope of previous methods, especially for coastal turbid waters (Mao et al., 2018; Jiang et al., 2019; Zhao et al., 2022). The Z_{sd} in complex coastal waters is more unstable compared to oceanic water which greatly increases the difficulty of monitoring.

To accurately invert the Z_{sd} for complex water, various inversion methods based on water body classification have been proposed in previous studies. For instance, Liu et al. and Xiang et al. classified water into clear to moderately turbid water and highly turbid water, and clear, moderately turbid, and highly turbid water based on remote sensing reflectance band ratios, respectively, and used corresponding algorithms to estimate Z_{sd} (Liu et al., 2022; Xiang et al., 2023); Jia et al. established an inversion method for water with different nutrient states based on the fuzzy logic optical water type scheme (Jia et al., 2022). These methods essentially rely on strict thresholds partitioning, although they perform well in obtaining Z_{sd} of turbid water. In fact, the boundary between clarity and turbidity in complex water is not very clear, and threshold division may result in discontinuity of Z_{sd} estimation results near the threshold (Yu et al., 2019). For this reason, we improved the semi-analytical model (Lee15) by leveraging QAA_{clear} and QAA_{turbid} to simulate the continuous changes in water Z_{sd}, thereby avoiding the constraints of fixed thresholds and ensuring data continuity (Lee et al., 2015; Chen et al., 2022). Given the complexity and continuous variability of nearshore water, we have chosen the improved model for inversion in order to obtain more accurate Z_{sd} information.

Moreover, current studies primarily focus on the inversion of characteristics in inland lakes, open oceans, and coastal bays (Shi and Wang, 2012; Mao et al., 2018; Zhou et al., 2021). Studies specifically addressing turbid coastal waters with varying optical properties are relatively scarce, particularly concerning long-term series analysis (Shang et al., 2016; Guo et al., 2022, 2023a). To advance our understanding of long-term changes in complex nearshore waters, we generate daily Z_{sd} data with spatial resolution of 1 km by inverting the Z_{sd} within 100 km of coastal waters in eastern China from 2003 to 2023 using an improved algorithm based on modified secondary water bodies. The principal objectives of this research are as follows: (1) to reveal the long-term spatiotemporal distribution pattern of Z_{sd} within 100 km of coastal waters in eastern China; (2) to elucidate the spatiotemporal distribution characteristics and key influencing factors of Z_{sd} in typical estuaries in eastern China. These results not only provide high-resolution data for the analysis of long-term Z_{sd} changes in coastal waters of China, but also offer a novel perspective for a deeper understanding of the spatiotemporal variation in seawater Z_{sd}.

2 Data and methods

2.1 Study area

The study area extends 100 km inland from the eastern coast waters of China, encompassing the BS, the YS, and the northern area of the ECS (Figure 1). It spans latitudes 25.3° to 41.0°N and

longitudes 117.6° to 125.4°E, covering a total area of approximately 376,937 km² with an average depth of 31.55 m. The coastal waters serve as recipients for numerous rivers originating from the mainland, which consistently transport sediment and other nutrients to the ocean (Dai et al., 2018). Among these rivers, the Yangtze River stands as China's largest river, annually conveying approximately 5.0× 10^8 million tons of sediment to the ECS. Additionally, the Yellow River ranks as China's second largest river, transporting around 1.1×10^9 tons of sediment to the BS each year (Milliman and Meade, 1983). Other major rivers, including the Liaohe, Qiantang, Haihe, and Minjiang rivers, also contribute substantial quantities of sediment to these three seas (Shi and Wang, 2012). The impact of these sediments on nearshore Z_{sd} is of significant consequence. A substantial quantity of sediment from the Liaohe and Yellow Rivers has been transported and deposited in the BS, resulting in the formation of two delta wetlands: the Liao River Estuary and the Yellow River Estuary. The identification of sediments from the ancient Yellow River as a contributing factor in the formation of the Subei Shoal, situated in the vicinity of Jiangsu Province, China, has been made in the YS (Shi and Wang, 2012). Concurrently, a considerable quantity of sediment from the Yangtze River and the Qiantang River, in conjunction with the river's interaction with the sea, has resulted in the formation of a substantial tidal delta and a trumpet-shaped Hangzhou Bay on the west coast waters of the ECS (Hori et al., 2002). As the largest mountain river on the southeast coast, the Minjiang River contributes a significant amount of sediment to the region, forming a medium-sized high-tide estuarine system and a delta with distinct sedimentary zones (Wu et al., 2023).

2.2 Data sources

The R_{rs} data at 412 nm, 443 nm, 488 nm, 531 nm, 547 nm, 555 nm, and 667 nm, taken at a spatial resolution of 1 km × 1 km with daily temporal resolution, were derived from the MODIS-Aqua level 2 data of the NASA Ocean Biology Processing Group (OBPG, https://oceancolor.gsfc.nasa.gov/), covering the period from 2003 to 2023. To enhance data quality, we performed rigorous quality control on all MODIS R_{rs} data, including using quality assurance (QA) bands to remove interference from factors such as clouds and aerosol particles, and removing negative values. The bathymetric data were derived from ETOPO 2022 (https://www.ncei.noaa.gov/products/etopo-global-relief-model), a global bathymetric topographic elevation dataset released by the National Environmental Information Center of the United States in 2022.

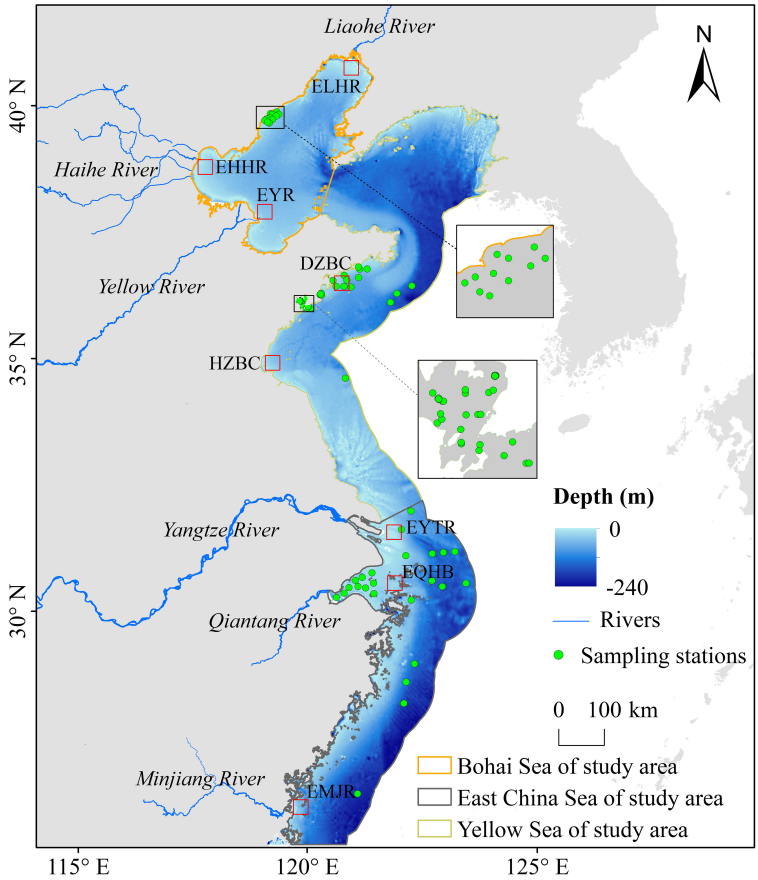

FIGURE 1
Study area. ELHR, the Estuary of Liaohe River; EHHR, the Estuary of Haihe River; EYR, the Estuary of Yellow River; DZBC, The Dingzi Bay and Coast; HZBC, The Haizhou Bay and Coast; EYTR, the Estuary of Yangtze River; EQHB, the Estuary of Qiantang River and Hangzhou Bay; EMJR, the Estuary of Minjiang River.

The dataset of *in situ* Z_{sd} was obtained from the National Field Scientific Observation and Research Station of the Jiaozhou Bay Marine Ecosystem in Shandong Province (http://jzb.cern.ac.cn/), the National Earth System Science Data Center (https://www.geodata.cn/main/), and relevant references (Zheng et al., 2014; Fang et al., 2021; Zhan et al., 2021; Zhang et al., 2022). The dataset includes 225 sets of matched data from 84 sampling stations, spanning from 2005 to 2020, with locations ranging from 120.79°E to 123.80°E and 26.39°N to 36.77°N (Figure 1). The data on annual runoff and sediment transport volume for the Liao River, Haihe River, Yellow River, Yangtze River, Qiantang River, and Minjiang River were obtained from the River Sediment Bulletin of China (2003-2023, China Water Power Press) (http://www.mwr.gov.cn/sj/tjgb/zghlnsgb/). The data presented here were obtained from representative hydrographic stations located in close proximity to the estuaries and are detailed in Supplementary Table S1.

2.3 Methods

2.3.1 Algorithm to retrieve

Z_{sd}Lee et al. developed a quasi-analytical algorithm for retrieving the inherent optical properties of water (Zhan et al., 2020). They subsequently refined the algorithm multiple times for different types of water, resulting in the successive proposals of QAA-v4, QAA-v5, and QAA-v6 (Zhan et al., 2020). Proposed in 2015, QAA-v6 is a semi-analytic algorithm developed based on a new underwater visibility theory for the $a(\lambda)$ and $b_b(\lambda)$ of water from visible spectra (Lee et al., 2015). Then, the $K_d(\lambda)$) was estimated from a and b_b with Lee's K_d model (Lee et al., 2015; Xiang et al., 2023). A total of seven bands in the visible spectrum of the MODIS sensor were selected for the estimation of Z_{sd} in coastal waters in this study. These include the following wavelengths: 412 nm, 443 nm, 488 nm, 531 nm, 547 nm, 555 nm, and 667 nm. Of these, 555 nm was chosen as the reference band. The estimate of K_d can be expressed as (Lee et al., 2015):

$$K_d(\lambda) = (1 + 0.005 \times \theta_s)a(\lambda) + (1 - 0.265\frac{b_{bw}(\lambda)}{b_b(\lambda)}) \times 4.26 \times (1 - 0.52 \times e^{-10.8\times a(\lambda)})b_b(\lambda) \quad (1)$$

Where $K_d(\lambda)$ is the diffuse attenuation coefficient; $a(\lambda)$ is the absorption coefficient of the total; $b_b(\lambda)$ is the backscattering coefficient of total and $b_{bw}(\lambda)$ is the backscattering coefficient of pure seawater; θ_s is the solar zenith angle.

Then, the Z_{sd} was estimated from $K_d(\lambda)$ and $R_{rs}(\lambda)$ using the following formula (Lee et al., 2015):

$$Z_{sd} = \frac{1}{2.5Min(K_d(412, 443, 488, 531, 547, 555, 667))} ln(\frac{|0.14 - R_{rs}^{PC}|}{0.013}) \quad (2)$$

where $Min(K_d)$ represents the minimum diffuse attenuation coefficient of the 412 nm, 443 nm, 488 nm, 531 nm, 547 nm, 555 nm, and 667 nm bands in coastal waters. R_{rs}^{PC} denotes the remote sensing reflectance in the same band as the minimum K_d.

In accordance with the value of the water $R_{rs}(670)$, QAA-v6 subdivides the water into two models for calculation, which are the clear water model (QAA_{clear}) and the turbid water model (QAA_{turbid}) (Lee et al., 2015). Most coastal waters in the BS, YS, and ECS are classified as Class II water bodies. QAA_{clear} may underestimate the Z_{sd} of some clear water, while QAA_{turbid} may overestimate the Z_{sd} of some turbid water (Feng et al., 2019). Consequently, for turbidity and fast-changing Class II water bodies, the threshold of $R_{rs}(670)$ can be adjusted in order to circumvent the problem of underestimation in clear water and overestimation in turbidity water (Qiu et al., 2023). To estimate the Z_{sd} of coastal waters with greater accuracy, our improved model based on Lee15 was performed (Chen et al., 2022). The improved model postulates that the Z_{sd} is uniform between the turbid and clear states. According to the characteristics of this process, we fitted the model with a binary logistic regression model (Chen et al., 2022). When Z_{sd} is extremely low, the ratio of QAA_{clear} is 0; In turn, when Z_{sd} is extremely high, the ratio of QAA_{clear} is 1. Moreover, the coefficient of QAA_{clear} is used to construct a logistic function. It can be expressed as:

$$C_{clear} = 1/(1 + e^{-k(Z_{sd_{clear}} - x_0)}) \quad (3)$$

where C_{clear} and $Z_{sd_{clear}}$ are the proportion and the Z_{sd} estimation of QAA_{clear}, k and x_0 are the steepness and the x value of the midpoint of the curve, and the sum of the proportion of QAA_{turbid} and QAA_{clear} should be one.

Subsequently, we refined the parameters by fitting the curve using the least squares method based on the Z_{sd} of 106 matched field measurements and spectral estimates. After that, by calculating the curvature of the curve to find the position of the threshold, and use Formula 3 and Lee15 to derive C_{clear} and C_{turbid}. The coefficients of the two models used in this study are from our previous research (Chen et al., 2022). Finally, the Z_{sd} can be expressed as follows:

$$Z_{sd} = C_{clear} \times Z_{sd_{clear}} + C_{turbid} \times Z_{sd_{turbid}} \quad (4)$$

where C_{clear} and C_{turbid} are the coefficients of QAA_{clear} and QAA_{turbid}; $Z_{sd_{clear}}$ and $Z_{sd_{turbid}}$ are the estimations of Formula 2.

2.3.2 Accuracy assessment

In this study, the accuracy verification process is as follows: (1) we matched and compared the Z_{sd} obtained by using Lee15 and the improved model with the measured Z_{sd} data, respectively. (2) in order to obtain more matched data, we set the time window of daily data to 24 h and defined the spatial window as the Z_{sd} of the pixel in which the station is located or eight adjacent pixels, resulting in a total of 225 pairs of matched data. In addition, the accuracy tests conducted in this study employed the following indices: R^2 (Coefficient of Determination), Root Mean Square Error (RMSE) and Mean Absolute Error (MAE). The RMSE and MAE are calculated using the following formulas:

$$RMSE = \sqrt{\frac{1}{N}\sum_{i=1}^{n}(y_i - \hat{y}_i)^2} \quad (5)$$

$$MAE = \frac{1}{N}\sum_{i=1}^{n}|y_i - \hat{y}_i| \quad (6)$$

In these formulas, y_i and $\hat{y}_i$ represent the Z_{sd} measured and estimated values of the sample i. N represents the total number of samples, which in this study is equal to 225.

2.3.3 Mann-Kendall trend test

The Mann-Kendall trend test is a nonparametric test model widely employed in the analysis of time series for trends and abrupt changes (Subash et al., 2011). This test method does not require a specific sequence distribution and is not sensitive to anomalies. The process of the Mann-Kendall trend test is as follows: for the sequence $X_i = (x_1, x_2,\ldots, x_n)$, the size relationship between x_i and x_j in all dual values (x_i, x_j, $j > i$) (set as S) must first be determined, and then a significance test must be performed on it. The test statistic formulas are as follows:

$$S = \sum_{i=1}^{n-1}\sum_{j=i+1}^{n} Sgn(x_j - x_i) \tag{7}$$

$$Sgn(x_j - x_i) = \begin{cases} +1, & x_j - x_i > 0 \\ 0, & x_j - x_i = 0 \\ -1, & x_j - x_i < 0 \end{cases} \tag{8}$$

In addition, the choice of significance test statistics is contingent on the length of the time series. Given that the time series in question has a length of 21 years (2003-2023), it can be reasonably assumed that the statistical statistic S approximately follows a standard normal distribution. Accordingly, the significance test is performed using the test statistic Z, which is calculated in accordance with Formulas 9 and 10.

$$Z = \begin{cases} \frac{S-1}{\sqrt{Var(S)}}, & S > 0 \\ 0, & S = 0 \\ \frac{S+1}{\sqrt{Var(S)}}, & S < 0 \end{cases} \tag{9}$$

$$Var(\mathrm{S}) = ((n-1)(2n+5) - \sum_{i=1}^{m} t_i(t_i-1)(2t_i+5))/18 \tag{10}$$

In Formulas 9 and 10, n represents the number of data points in the sequence, m denotes the number of knots (repeated data groups) in the sequence, t_i is the width of the knots (number of repeated data points in the group i), and $Var(S)$ is the variance of S. During the test, the significance level is taken as $\alpha = 0.05$, and $Z_{1-\alpha/2} = Z_{0.975} = 1.96$. When $|Z| \le 1.96$, the trend is not considered to be significant; if $|Z| > 1.96$, the trend is considered to be significant. Moreover, if $Z > 0$, the sequence is considered to have an upward trend, and if $Z < 0$, the sequence is considered to have a downward trend.

2.3.4 Sen's slope estimation

Sen's slope, also known as Sen's slope estimation, represents a nonparametric approach to computing the trend slope. The slope indicates the amplitude of the variability in the Z_{sd} of the series. The Sen's trend represents the median of the calculated sequence, which effectively reduces the impact of noise and is not affected by the singular values of the sequence. The Sen's slope is an effective method for reflecting the extent of change in the trend of a sequence. However, it is not a standalone indicator of trend significance and can be assessed in conjunction with the Mann-Kendall trend test method (Burn and Elnur, 2002), which has a wide range of applications in the analysis of hydrometeorological data (da Silva et al., 2015). For a time series $X_i = (x_1, x_2,\ldots, x_n)$, the Sen's slope estimates of the trend β are calculated as follows:

$$\beta = median\frac{x_j - x_i}{j - i} \forall j > i \tag{11}$$

The median is the median function, and when β>0, the time series shows an upward trend; When β<0, the time series shows a downward trend.

2.3.5 Calculation of mean and anomaly

The temporal and spatial means and anomalies of various properties are commonly employed to elucidate spatio-temporal variations in geophysical properties (Shang et al., 2011). This approach allows us to calculate the monthly, quarterly, annual, and multi-year spatial mean and temporal anomaly of Z_{sd}, respectively. The exact calculation is as follows: for a given pixel i of an extracted month in an extracted year, the monthly average of Z_{sd} is calculated by adding all valid values for each day of the month and dividing them by the number of valid days. The calculation of annual average is the sum of the average values of all valid months in a year, and then divided by the number of months with valid values. Similarly, the multi-year monthly average is the sum of the monthly average effective value of Z_{sd} for pixel i from 2003 to 2023 divided by the number of months in which the effective value exists. Multi-year quarterly average is obtained from quarterly statistics based on the multi-year monthly average in a similar way. Time anomalies count the difference between a month in a given year and the long-term average for that month. This can reflect the anomaly of that month in a given year with respect to the long-term average. The methods employed to calculate these averages and anomalies are outlined in detail in Shang et al. (2011).

3 Results

3.1 Evaluation of Z_{sd}

Following a series of processing steps, including projection, clipping and quality control band screening, all MODIS R_{rs} data are calculated in Matlab using the Lee15 and the improved model, with the objective of obtaining the daily Z_{sd} of the area within 100 km of the east coast of China. After the data cleaning process, a total of 225 pairs of data were used for accuracy verification. The results demonstrate that the RMSE and MAE of the improved algorithm have decreased from 1.49 to 1.32 and from 0.96 to 0.94 when compared to the Lee15, respectively (Figures 2A, C). More importantly, the coefficient of determination R^2 increased from 0.63 to 0.70 (Figures 2A, C). The improvement of these indicators indicates that our model has better adaptability when dealing with high turbidity water. Moreover, to demonstrate the strength of the improved model, we compare it with the new three-class model, using the similarity principle (Xiang et al., 2023). This new three-class model, which classifies water as clear, extremely turbid, and moderately turbid water, employs the Lee15, simple semi-analytical, and weighted average methods, respectively. The accuracy of this

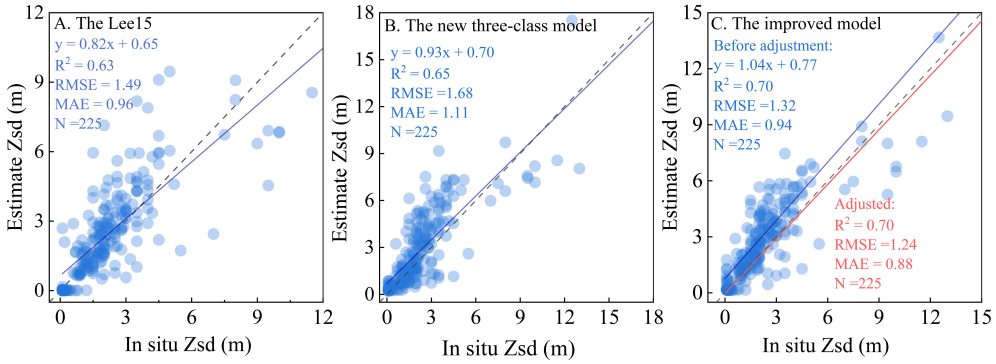

FIGURE 2
(A) *In situ* Z_{sd} compared to Z_{sd} derived from MODIS R_{rs} using the Lee15. **(B)** *In situ* Z_{sd} compared to Z_{sd} derived from MODIS R_{rs} using the new three-class model. **(C)** *In situ* Z_{sd} compared to Z_{sd} derived from MODIS R_{rs} using the improved model and Z_{sd} estimated (bias corrected).

model is still inferior to ours, with an R^2 of 0.65, RMSE of 1.69 and MAE of 1.11 (Figure 2B). These results further solidify the reliability of our improved model for handling complex water. Consequently, the improved algorithm exhibits superior performance, whereas the Lee15 may have erroneously classified turbid water as clear water in the Z_{sd} estimation, resulting in an overestimation of Z_{sd}.

Furthermore, Figure 2B illustrates that the *in situ* measured Z_{sd} appears to be consistently lower than the estimated Z_{sd}. The slope is 1.04, which is close to 1, indicating a discrepancy between the fitted line and 1:1 line. This discrepancy may be attributed to differences in sample size and measurement time (Feng et al., 2019). Therefore, the correlation between the two variables can be used to adjust the bias in the Z_{sd} estimate. The correlation can be expressed as follows:

$$Z'_{sd} = \frac{Z_{sd,estimate} - 0.77}{1.04} \tag{12}$$

It can be further expressed as follows:

$$Z'_{sd} = 0.96 \times Z_{sd,estimate} - 0.74 \tag{13}$$

Following calculation, the adjusted model has a MAE of 0.88, RMSE of 1.24, and R^2 of 0.70, indicating an improvement in accuracy compared to the before adjustment model. Therefore, this study used the improved model to invert Z_{sd} and adjusted the results according to Formula 13, thereby making them more closely aligned with the true Z_{sd}.

3.2 Spatial and temporal distribution of Z_{sd} in the coastal waters within 100 km of China during 2003-2023

3.2.1 Spatial variation of Z_{sd}

To elucidate the long-term spatial variation of Z_{sd} within 100 km coast waters of eastern China, we calculated the annual average Z_{sd} based on the retrieved daily Z_{sd}, with spatial resolution of 1 km (Figure 3). The results indicated that the average Z_{sd} was 1.32 m from 2003 to 2023. On the whole, Z_{sd} showed an increasing trend with the increase of coastal distance. In particular, regions with high values of Z_{sd} were concentrated in the north of the YS, south of Shandong Peninsula, and the far coast of the ECS, while regions with low values of Z_{sd} were mainly in the BS, the northern coastal zone of Jiangsu (NJCZ), and the nearshore of the ECS. Moreover, seawater adjacent to the shoreline has a consistently lower Z_{sd} due to its greater impact from runoff inputs, more complex hydrodynamics, and stronger human activity compared to the ocean, resulting in a higher probability of sediment resuspension (Zhao et al., 2023). Meanwhile, the Z_{sd} in the ECS exhibited typical circular distribution characteristics, and the Z_{sd} in the NJCZ did not show considerable variation with increasing distance from the coast, forming a tongue-shaped low Z_{sd} area.

3.2.2 Interannual variation of Z_{sd}

Sen's slope estimation and Mann Kendall significance test were performed to explore the interannual trend of Z_{sd} in the study. The results indicated that the number of pixels with significant increase, significant decrease, and no significant variation in Z_{sd} from 2003 to 2023 accounted for 20.84%, 1.14%, and 78.02% of the study area, respectively (Figure 4; Supplementary Table S2). This indicates that Z_{sd} has remained relatively stable over the past 21 years for most of the area within 100 km of the eastern coast of China, and that regions with significantly increased Z_{sd} are much larger than those with significantly decreased Z_{sd}. Specifically, the regions with significantly increased Z_{sd} mainly belong to northern China, including the coastal waters of the BS and the northern YS, while the regions with significantly decreased Z_{sd} are the DZBC and HZBC of the YS. In contrast, the sea regions with insignificant variation in Z_{sd} include the ECS, the southern and central YS, and the central and northern BS (Figures 4A, B). These variations in Z_{sd} in coastal waters further indicate a trend of improving water quality along the northern coast of China during the period 2003 to 2023.

Furthermore, we calculated the anomalies of Z_{sd} in three sea areas to investigate whether there is a periodic pattern of variations. The results showed that the anomalies of Z_{sd} in the BS and YS exhibited a significant increase trend in the past 21 years ($p = 0.002$ and $p = 0.025$, respectively), with an average increase of 0.009 m/year and 0.007 m/year, respectively (Figures 5A, B). However, some Z_{sd} anomalies in the ECS demonstrated an insignificant change ($p = 0.188$; Figure 5C). Concurrently, the anomalies of Z_{sd} in different

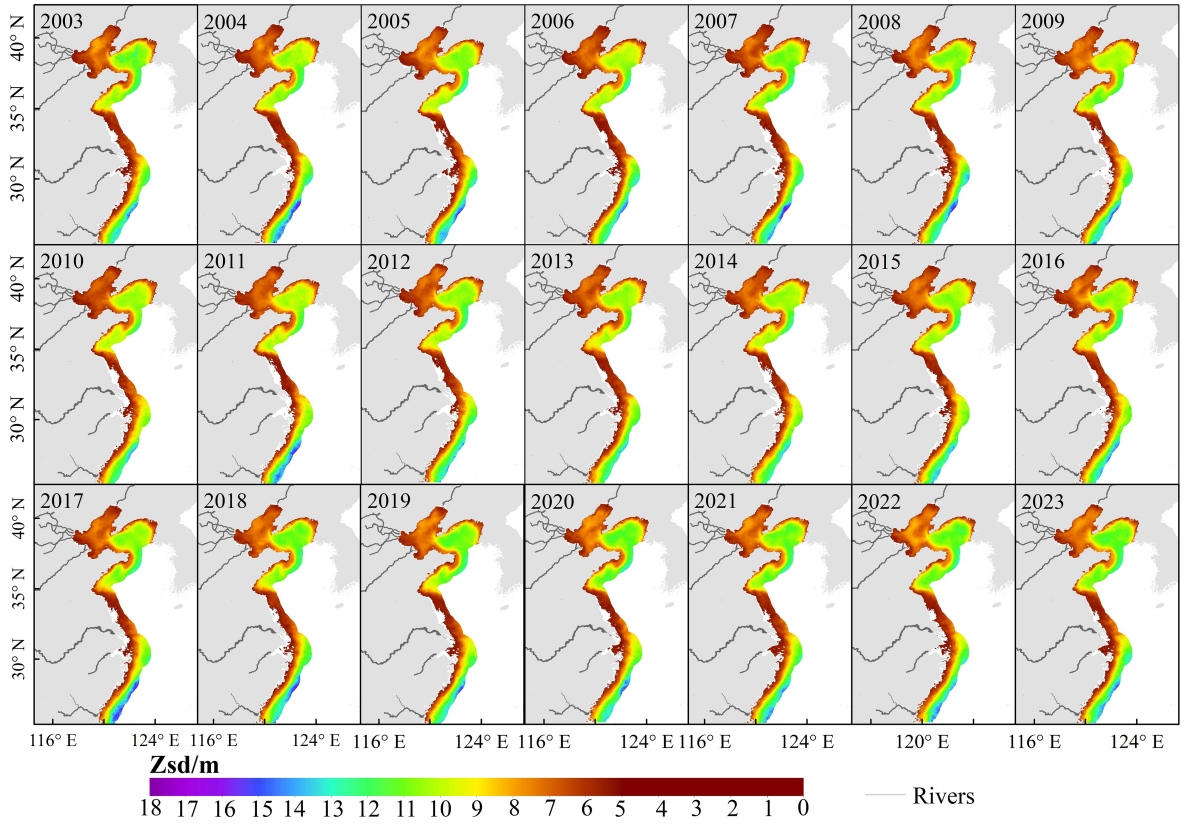

FIGURE 3
Spatial distribution of annual Z_{sd} within 100 km of the eastern coast of China from 2003 to 2023.

seas showed a phased pattern of change. In detail, the BS can be divided into three stages, with Z_{sd} significantly decreasing from January 2003 to August 2007 ($p = 0.001$), while there was no significant variation from September 2007 to December 2015 ($p = 0.381$), and significantly increasing from January 2016 to December 2023 ($p < 0.0001$) (Figure 5A). The YS can be divided into two stages, with no significant change in Z_{sd} between January 2003 and July 2009 ($p = 0.498$), and a significant increase between August 2009 and December 2023 ($p < 0.0001$) (Figure 5B). Although there has been a slight increase in Z_{sd} in the ECS on the whole, there has not been a significant variation ($p = 0.188$; Figure 5C), which is due to the large fluctuations in Z_{sd} during the year. Overall, the Z_{sd} anomalies in the BS and YS have increased significantly over the past 21 years, while there is no significant variation in the ECS, and the anomalies in Z_{sd} in different seas exhibit different phases of the variability pattern.

3.2.3 Seasonal and monthly variation of Z_{sd}

To clarify the long-term seasonal variability trend of Z_{sd}, this study calculated the monthly and quarterly average Z_{sd} for a 100 km sea area along the eastern coast of China from 2003 to 2023 based on the daily Z_{sd} product. As can be seen in Figure 6, the Z_{sd} of coastal waters had a conspicuous seasonal variation, with the performance being summer (mean = 1.81 m) > autumn (mean = 1.33 m) > spring (mean = 1.21 m) > winter (mean = 0.87 m). Specifically, in spring, the Z_{sd} of the BS, YS and ECS coastlines, as well as NJCZ, was lower than 4 m, while the Z_{sd} of the northern YS, southern Shandong Peninsula, and far shore of the ECS was higher, reaching 12 m. By summer, Z_{sd} increased compared to spring, with the highest values of Z_{sd} reaching 8 m, 12 m and 16 m in the BS, YS, and ECS, respectively. Subsequently, the Z_{sd} of seawater began to decrease in autumn. In winter, the Z_{sd} of all sea areas reached the lowest value of the year, with the smallest spatial differences and the highest Z_{sd} in the BS, YS, and ECS was less than 3 m, 9 m, and 12 m, respectively (Figure 6; Supplementary Table S1).

We further analyzed the monthly distribution of the maximum and minimum Z_{sd} for each pixel within 100 km of the eastern coast of China based on the monthly average products from 2003 to 2023 to gain a deeper understanding of the monthly variability of Z_{sd}. The results showed that the time interval between the maximum and minimum of Z_{sd} is usually ~6 months. Overall, Z_{sd} mainly reached maximum in June, July, or August (Supplementary Figure S2A), while reaching minimum in December, January, and February (Supplementary Figure S2B). Specifically, the maximum and minimum of Z_{sd} in the southern of the Shandong Peninsula appeared earliest in June and December, respectively (Supplementary Figure S2). Subsequently, the maximum of Z_{sd} in the coastal waters of the BS and the northern of the YS mainly occurred in July, while the minimum was in February. The maximum and minimum of Z_{sd} were both one month later than those in the central BS. Furthermore, the maximum Z_{sd} in the central and northern YS generally occurred in August, while the

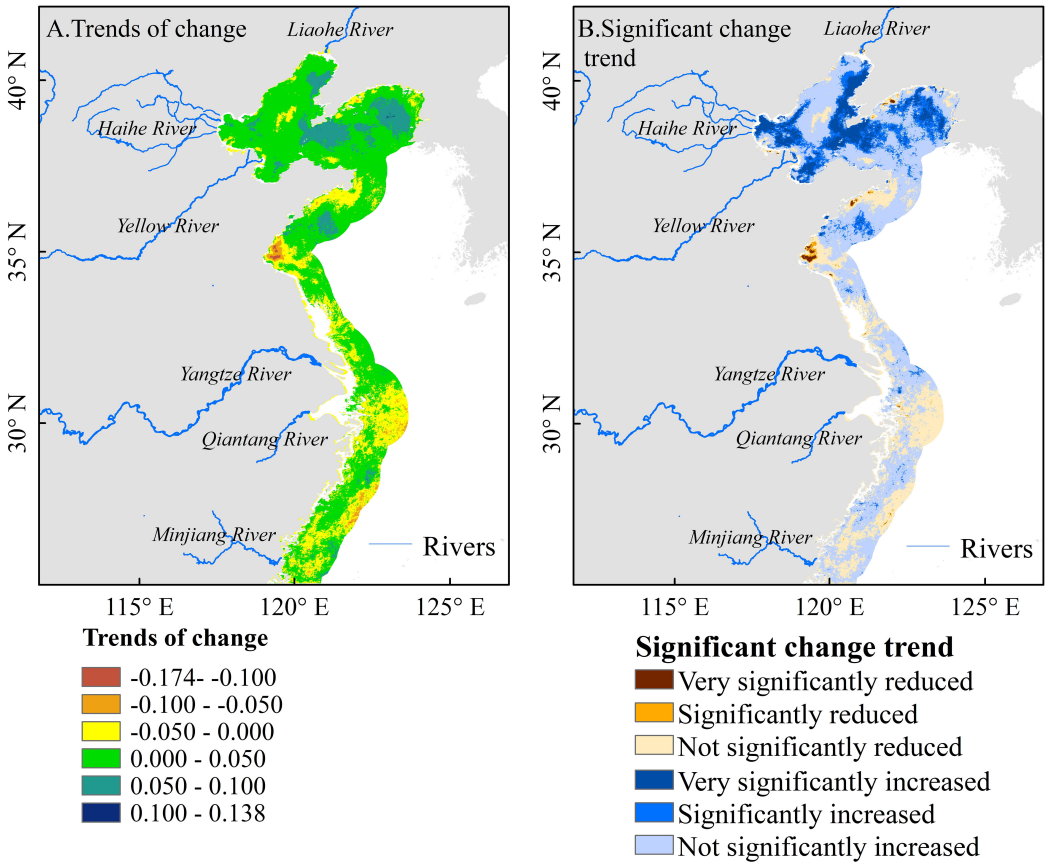

FIGURE 4
The distribution of annual variation trend of Z_{sd} within 100 km of the eastern coast of China **(A)**. The distribution of annual significance test of the Z_{sd} within 100 km of the eastern coast of China **(B)**.

minimum occurred in January. As for the ECS, the maximum of Z_{sd} occurred in June, August, or September, while the minimum was in January (Supplementary Figure S2).

3.3 Spatial and temporal distribution of Z_{sd} in six typical estuaries during 2003-2023

Estuaries are important channels for the ocean to receive runoff and sediment, and their Z_{sd} is strongly influenced by the interaction between the ocean and the land environment (An et al., 2023). The rivers corresponding to ELHR, EHHR, EYR, EYTR, EQHB, and EMJR are the main rivers in China, spanning different climate zones and geological conditions along the eastern coast of China, as well as in the areas with the highest intensity of human activities. In addition, these estuaries receive 69% of the runoff and 78% of the sediment input from China's land to the ocean. Therefore, these six estuaries have typical representativeness and the area with 32 km x 32 km of them were used to analyze the spatiotemporal variations of Z_{sd} (Figure 1). In order to explore the long-term trend of Z_{sd} in these estuaries, we calculated the annual average of each pixel from 2003 to 2023 and defined valid pixels as pixels with an average greater than 0 and sample size of no less than 15. The results showed that the EMJR had the highest average (2.64 m) of Z_{sd} from 2003 to 2023, followed by the EYR (1.65 m), EHHR (1.13 m), ELHR (0.73 m), and EQHB (0.66 m), while the average Z_{sd} of the EYTR was the lowest, at 0.64 m (Figure 7). On a long-term trend, the Z_{sd} of ELHR, EHHR, EYR, EQHB, and EMJR showed a significant increase, while there was no significant change in EYTR (Figure 7). However, the corresponding R^2 in EQHB and EMJR is at an extremely low level ($R^{2<}$ 0.02), although the change trends of their Z_{sd} is significant ($p< 0.05$; Figures 7E, F), which means that the actual explanation of time on Z_{sd} variation is weak, leading to statistically false positive results (Edwards et al., 2008). Therefore, the Z_{sd} of EQHB and EMJR is likely to have insignificant trend of change and belong to normal hydrological and meteorological fluctuations.

Furthermore, we calculated the monthly average Z_{sd} for each estuary from 2003 to 2023 to further understand the annual variation characteristics of Z_{sd}. The results showed that the Z_{sd} of ELHR, EHHR, EYR, and EMJR were the highest during the summer months of the year, with a single peak trend. By comparison, the EYTR and EQHB Z_{sd} exhibited a bimodal pattern with peaks in autumn and spring, with the highest Z_{sd} occurring in autumn. Moreover, the Z_{sd} of ELHR, EYTR, and EQHB fluctuated less within the year (Figures 8A, D, E), while the Z_{sd} of EHHR, EYR, and EMJR showed obvious seasonality and instability (Figures 8B, C, F).

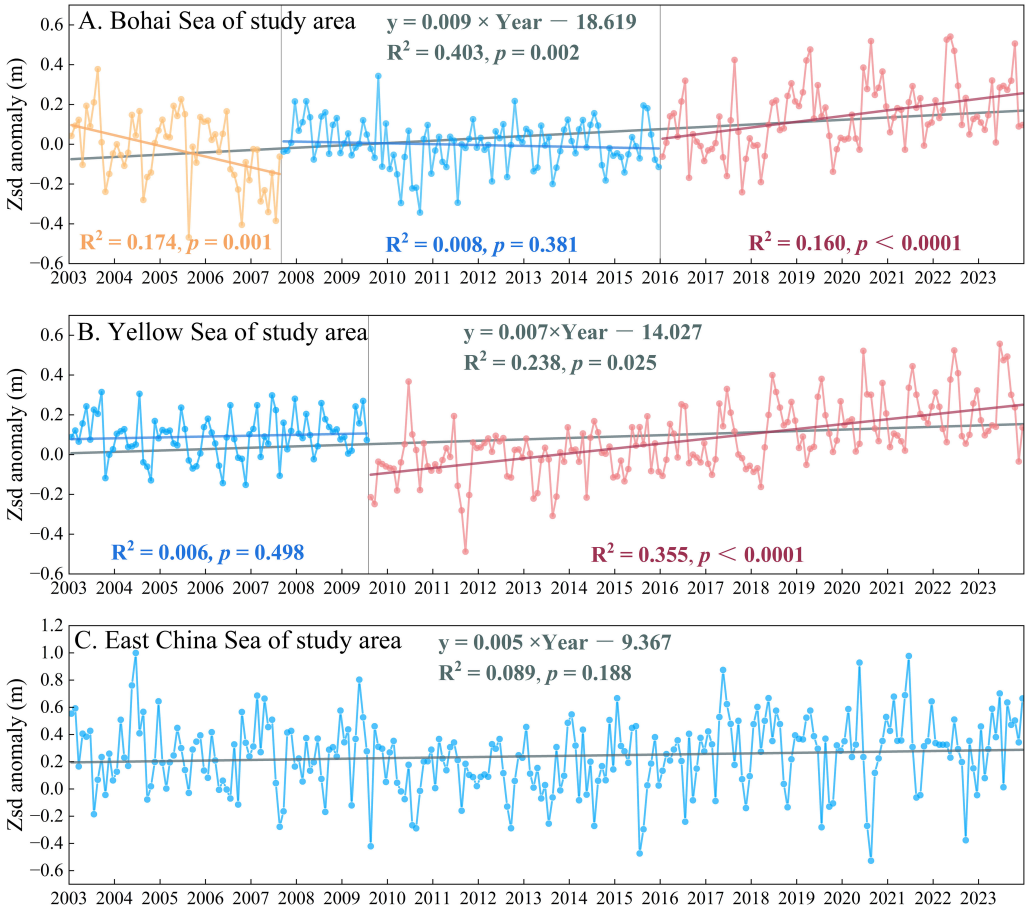

FIGURE 5
The time series and corresponding linear trends of the spatially averaged monthly Z_{sd} anomalies for the coastal areas within 100 km of the BS **(A)**, YS **(B)**, and ECS **(C)**.

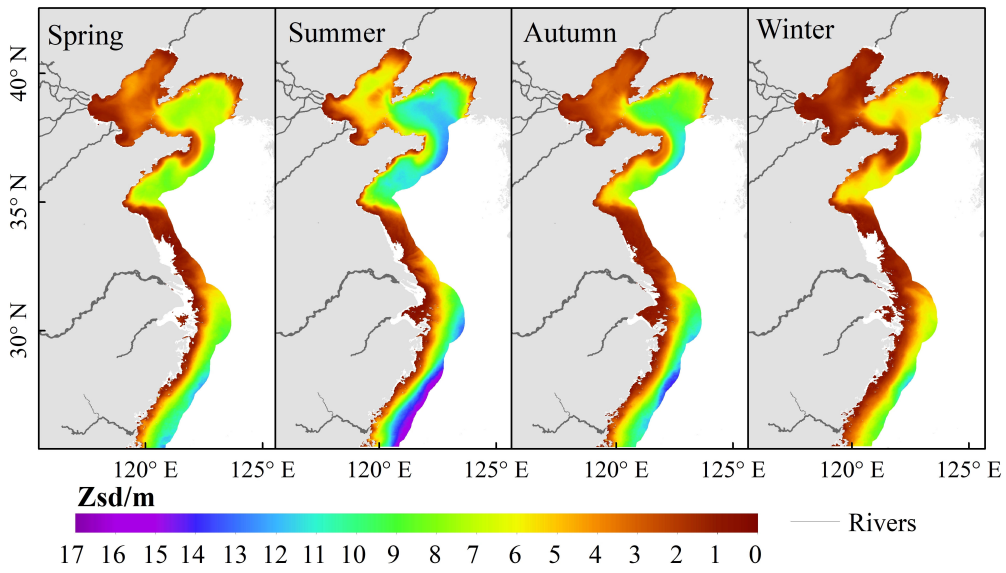

FIGURE 6
Spatial distribution of seasonal of Z_{sd} within 100 km of the eastern coast of China from 2003 to 2023.

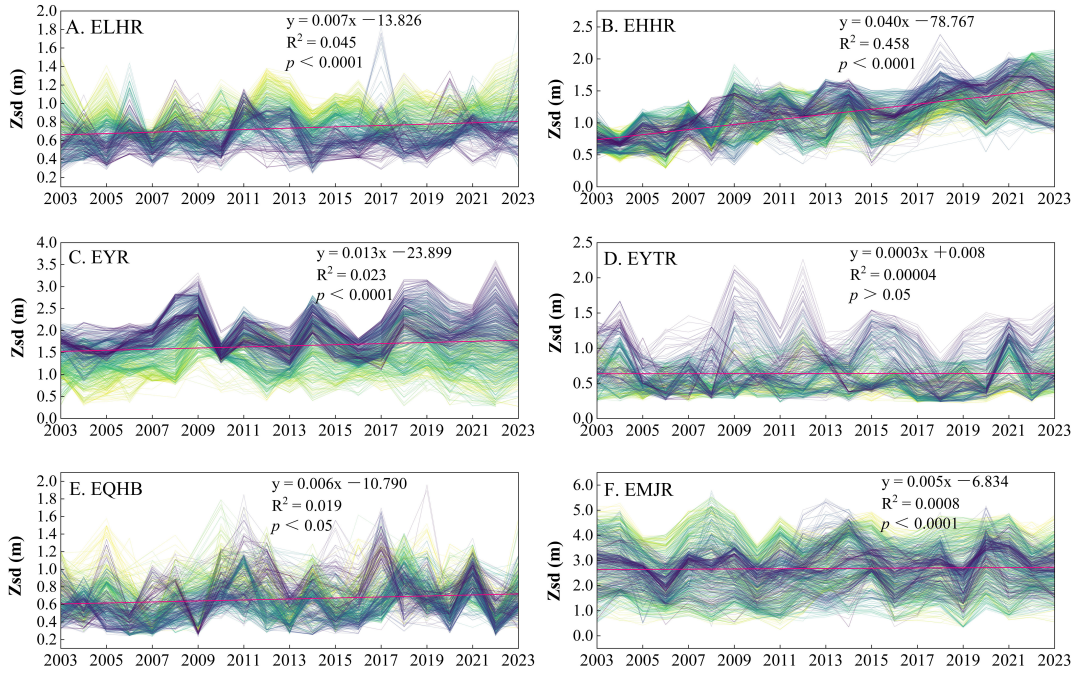

FIGURE 7
The interannual variations and linear trends of each pixel in the estuarine regions. Each line represents a single pixel, with darker colors indicating higher latitudes and lighter colors indicating lower latitudes. **(A–F)** represent ELHR, EHHR, EYR, EYTR, EQHB, and EMJR, respectively.

4 Discussion

4.1 Long-term drivers of Z_{sd} in the coastal waters within 100 km of China

Z_{sd}, as a significant indicator reflecting variation in water quality (Guo et al., 2023a), its attenuation process from top to bottom in natural water bodies is mainly dominated by the inherent optical properties (IOP) of water, including absorption coefficient and scattering coefficient. Under natural conditions, the main substances that affect two coefficients include colored dissolved organic matter (CDOM), suspended particulate matter (SPM), and phytoplankton (Shao et al., 2017; Zhou et al., 2021). Therefore, the reasons for variation of Z_{sd} can essentially be attributed to the effects of climate change, seawater dynamics, and human activities exerted through CDOM, SPM, and phytoplankton (Harvey et al., 2019; Zhou et al., 2021). Among them, phytoplankton is considered one of the most crucial influencing factors (Shao et al., 2017; Zhou et al., 2021). However, there is usually the highest density of phytoplankton in the summer (Gong et al., 2003; Yamaguchi et al., 2012), whereas the highest Z_{sd} remains at the same season (Figure 6), as well as in studies for seas of China (Guo et al., 2022, 2023a). Similarly, the lowest values of phytoplankton density and seawater Z_{sd} are observed simultaneously in winter (Figure 6) (Guo et al., 2022; Wang et al., 2023a). This phenomenon suggests that the driving effect of phytoplankton in coastal waters on long-term changes in Z_{sd} is secondary, while CDOM and SPM are dominant. The same phenomenon has also been observed in the Bothnian Sea, Baltic Sea, and Skagerrak (Harvey et al., 2019).

Our results suggest that the Z_{sd} of different seas in eastern China exhibited distinct change trends from 2003 to 2023, with a significant increase in Z_{sd} in the coastal waters of the BS and the north YS, while Z_{sd} in the DZBC and HZBC of the YS declined significantly, with no significant changes in other regions (Figures 4A, B). In the BS, the significant increase in Z_{sd} was related to the decline in SPM to a large extent, as in the past 21 years, the SPM of surface seawater in the BS had shown a decreasing trend against the background of weakened wind and wave intensity (Li et al., 2022), particularly in the southern region (Zhao et al., 2022). This phenomenon is in accordance with our results.

In the YS, the long-term variation of Z_{sd} in different regions exhibit different characteristics (Figures 4A, B). Among the regions, the northern region exhibits a significant increase in Z_{sd}, while the southwest regions of HZBC and DZBC exhibit a significant decrease. This is in line with the research results of Zhou et al. (2021) and Dong et al. (2011). The decrease in Z_{sd} of HZBC and DZBC from 2003 to 2023 can be attributed to sediment input and environmental pollution (Gao et al., 2023; Liang et al., 2023; Wang et al., 2024). Indeed, the excrement from industrial and agricultural production and aquaculture in the vicinity of these two areas has been continuously increasing since the 21st century (Pan et al., 2014; Liang et al., 2023). This puts tremendous pressure on the seawater. In one respect, the abundant nutrients can induce outbreaks of red and green tides, which can impede the penetration of light into seawater and reduce Z_{sd} (Liu et al., 2009). In another respect, a large amount of microplastics, as one of the suspended pollutants, can not only enrich CDOM and SPM, but also absorb and scatter light (Hoellein et al., 2019; Gao et al., 2023), this can all lead to a decrease in Z_{sd}. In addition, the DZBC is

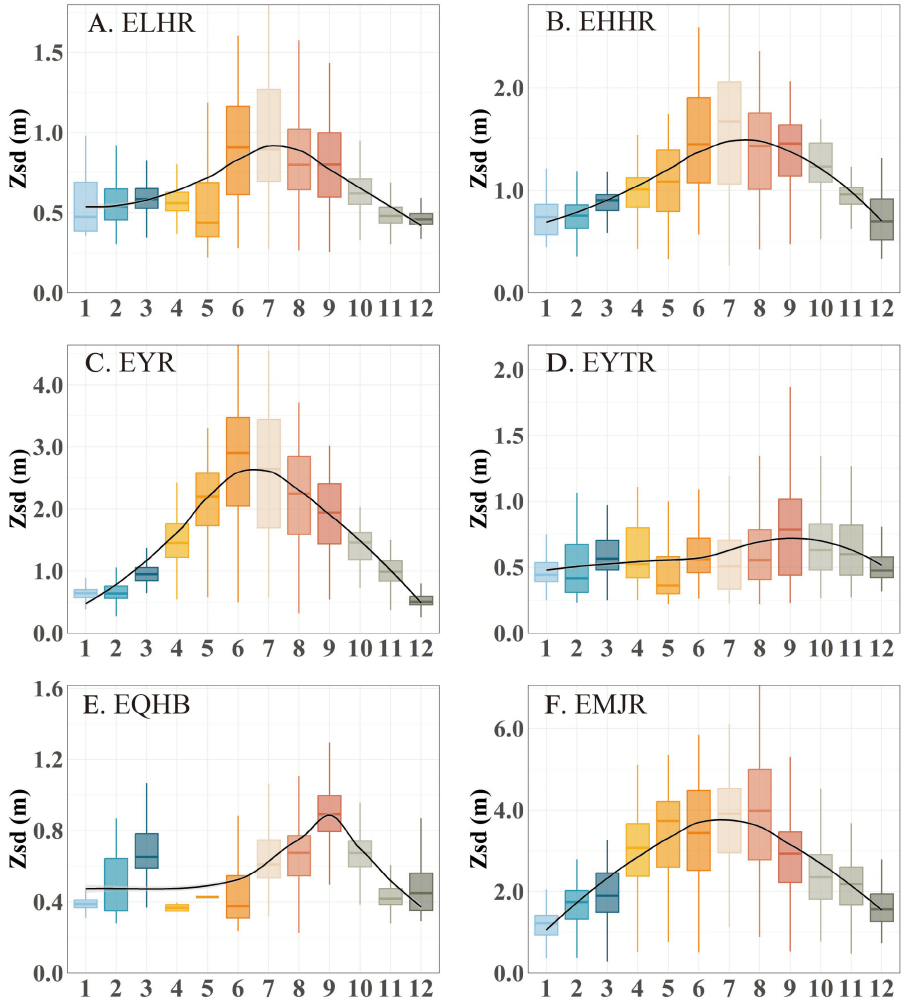

FIGURE 8
The Z_{sd} of the six estuaries changes during the year. **(A–F)** represent ELHR, EHHR, EYR, EYTR, EQHB, and EMJR, respectively.

located in a small muddy sediment area in the northwest of the South YS (Zhang et al., 2016), and recent coastal projects such as dredging and sand disposal can also promote further elevate the concentration of suspended sediments. It is noteworthy that, despite the seawater along NJCZ exhibiting minimal change in Z_{sd}, this has been the case for a long time. In truth, this region is situated between the old channel of the Yellow River Delta and the Yangtze River Delta, and a substantial amount of sediment accumulated in these deltas can significantly reduce Z_{sd} after suspension and diffusion (Rao et al., 2017; Su et al., 2017). At the same time, sediment from the Huai River can also contribute to the reduction of Z_{sd} (An et al., 2023). As a result, this area has become one of the most turbid coastal waters in China and has formed the famous Radial Sand Ridge (RSR), keeping its Z_{sd} at a low level year-round.

In terms of long-term seasonal variability, the Z_{sd} of coastal seawater is the highest in summer, followed by autumn and spring, and the lowest in winter. This change can mainly be attributed to seasonal variation patterns of temperature and wind. In summer, the increase in thermocline thickness caused by high temperatures enhances the vertical stability of water bodies, and the weak monsoon makes it difficult for the upper and lower layers of seawater to mix (Guo et al., 2023c), resulting in high Z_{sd}. In contrast, the thickness of the thermocline in winter decreases and the monsoon strengthens, which can promote the enhancement of vertical convection in seawater, thereby increasing the concentration of suspended solids (Shang et al., 2016; Mao et al., 2018; Guo et al., 2022), resulting in low Z_{sd}. Spring and autumn seasons are a transitional period between summer and winter, with relatively moderate temperature and monsoon intensity, so Z_{sd} is usually at the intermediate level. Furthermore, the seasonal variability of Z_{sd} shows an increasing trend with increasing offshore distance. This is due to the fact that coastal water bodies are more strongly affected by land runoff inputs, seawater dynamics (e.g., tides, waves, and coastal currents), and sedimentary suspension and transportation than far shore water bodies (Lewis et al., 1988; Megard and Berman, 1989; Idris et al., 2022).

4.2 Effects of runoff and sediment transport on the Z_{sd} of estuarine

In natural water bodies, CDOM and SPM are the two most important direct factors affecting Z_{sd} (Shao et al., 2017; Harvey et al., 2019; Zhou et al., 2021). However, due to the difficulty in obtaining large-scale and long-term CDOM and SPM data, we chose the sediment transport volume and runoff to indicate CDOM and SPM to reveal their effects on Z_{sd} variation in the six typical estuaries from 2003 to 2023. The results showed that there is spatial variation in the correlations between annual runoff and Z_{sd} to some extent: the Z_{sd} of estuaries in the northern region (ELHR, EHHR, and EYR) had a positive relationship with annual runoff (Figures 9A, C, E); while a negative relationship occurred in the southern region (EYTR, EQHB, and EMJR) (Figures 9G, I, K). Among them, Z_{sd} only significantly increases with the increase of annual runoff at the EHHR (Figure 9C), but significantly decreases with the increase of annual runoff at the EMJR (Figure 9K). This phenomenon cannot be separated from the increased intensity of human activity on the estuary. Since the 21st century, northern China has vigorously developed vegetation restoration projects and reservoir construction projects (Li et al., 2016). These ecological projects have the potential to effectively reduce the sediment transport of rivers (Wang et al., 2016). As the annual runoff increases, the water entering the estuary will be replaced more frequently, which helps to maintain the cleanliness of the water body and increase Z_{sd}. In contrast, South China has stronger industrial activity and denser population than north China (Liang et al., 2021), which means that rivers in the South will accept more pollutants and suspended solids and bring them into the estuary, leading to a decrease in Z_{sd} in the estuary.

For the relationship of annual sediment discharge and Z_{sd}, the Z_{sd} of EHHR, EYR, EYTR, EQHB, and EMJR were negatively correlated with their sediment transport volume, while a positive relationship was observed in ELHR (Figure 9). This result serves to reinforce the conclusion that an increase in sediment transport volume results in a reduction in the Z_{sd} of seawater. Notably, the annual runoff and sediment transport volume has a significant negatively correlation with Z_{sd} in EMJR ($p = 0.0056$, $p < 0.0001$) (Figures 9K, L). We believe that this phenomenon is mainly attributable to the relatively clear water of the EMJR (Figure 7). The concentration of SPM in the EMJR is lower than other turbid estuaries. The increase in EMJR sediment input significantly increased the concentration of SPM in the estuary, leading to a rapid decrease in Z_{sd} of EMJR with increasing annual runoff and sediment transport volume. However, the SPM concentration and eutrophication in turbid estuaries are usually at high levels, and the reduction of QAQ Z_{sd} requires more sediment and pollutants than in clean estuaries. Thus, the correlation between Z_{sd} and estuarine runoff as well as sediment transport is closely linked to the long-term cleanliness of estuarine water quality.

Additionally, we also observed that the Z_{sd} of the estuary shows a certain trend of variation with latitude (Figure 8). Hence, we further calculated their correlations. The results showed that the Z_{sd} of ELHR and EQHB significantly decreased with increasing latitude (all p values< 0.0001; Supplementary Figures S3A, E), whereas the Z_{sd} of

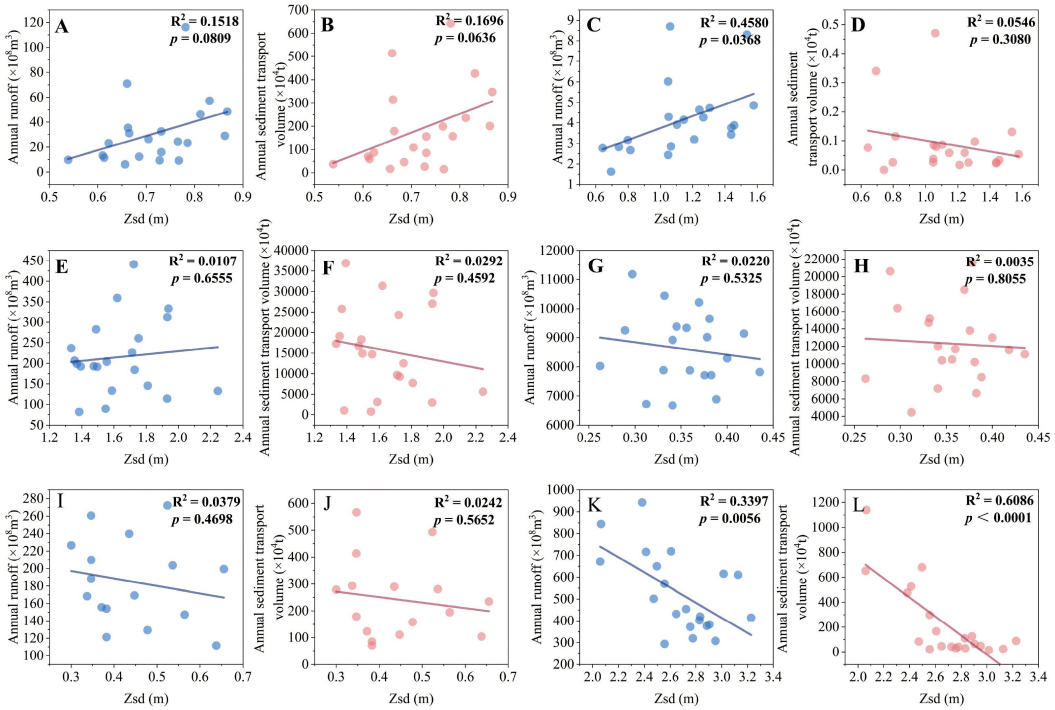

FIGURE 9
Correlations of estuary Z_{sd} with annual runoff and sediment transport volume in ELHR **(A, B)**, EHHR **(C, D)**, EYR **(E, F)**, EYTR **(G, H)**, EQHB **(I, J)**, and EMJR **(K, L)**.

EHHR, EYR, and EYTR were significantly increased with latitude (all p values< 0.0001; Supplementary Figures S3B-D), and the Z_{sd} of EMJR had no significant calculation with latitude (p = 0.0503; Supplementary Figure S3F). It is worth noting that although the relationship between Z_{sd} and latitude of EHHR and EQHB is significant (p< 0.0001), their corresponding R^2 is at a lower level (all R^2 values = 0.0283; Supplementary Figures S3B, E). This means that the effect of latitude on the Z_{sd} of EHHR and EQHB probably be weak. Actually, the effect of latitude on Z_{sd} is still dominated by the offshore distance of the seawater. On the one side, the sediment transport direction at the ELHR is from north to south (Figure 1), which means that the higher the latitude of the seawater, the closer it is to the shore, thereby synchronously reducing Z_{sd}. On the other side, the EYR we have chosen is located on the north bank of the estuary (Figure 1), so the higher the latitude, the farther offshore the seawater is, and the corresponding increase in Z_{sd}. In addition, the selected EYTR gradually moves away from Shanghai (China's economic center) from south to north (Shi and Liu, 2018), resulting in the increased Z_{sd}.

4.3 Importance and limitations

The deteriorating ecological health of coastal waters has become one of the obstacles to sustainable development in China. In this study, an improved model was used to invert and analyze the Z_{sd} and its spatiotemporal variations in coastal waters within a 100 km of eastern China from 2003 to 2023. Our results provide more accurate and continuous estimates of Z_{sd} for nearshore turbid waters compared to those obtained by the original model, so the dataset also has important application value in marine ecological protection and fishery production. In addition, this study has achieved considerable advance in both spatiotemporal resolution and time series length than the previous studies. In particular, the daily Z_{sd} data with a spatial resolution of 1km we obtained provides a reliable basis for in-depth research on the dynamic changes of nearshore water bodies. Furthermore, considering the estuary as the intersection of ocean and land, our analysis of the Z_{sd} changes and driving factors of typical estuaries can provide novel insights for scientific management and ecological restoration of estuaries at different latitudes.

However, there are still some limitations to this study. For example, although the R_{rs} data we use can cover the major area, there is a possibility of atmospheric correction failure in waters with an extremely high turbidity, resulting in a smaller amount of effective data being obtained (Guo et al., 2023a). Therefore, the improvement of atmospheric correction algorithms, the utilization of hyperspectral and multispectral data, and the fusion of multi-source spatiotemporal data should be the priority in the future. In addition, the Z_{sd} of seawater is not only directly affected by CDOM, SPM, and phytoplankton, but also indirectly disturbed by hydrodynamic and climatic factors (Lewis et al., 1988; Megard and Berman, 1989; Idris et al., 2022). Nevertheless, this study only quantificationally analyzed the effects of these direct influencing factors on Z_{sd}, making it difficult for us to fully comprehend the spatiotemporal variability pattern of seawater Z_{sd}. Consequently, we should consider the coupling relationship among multiple factors to further clarify the inherent mechanism of variation in seawater Z_{sd}.

5 Conclusion

In this study, we employed an improved model based on Class II water bodies to first invert the Z_{sd} of the coastal waters within 100 km of eastern China from 2003 to 2023 with a spatial resolution of 1 km. Our results achieve a higher accuracy in calculating Z_{sd} for offshore seas than those derived from the Lee15. On the whole, Z_{sd} showed an increasing trend with increasing coastal distance. The high Z_{sd} were located in the northern Yellow Sea, the southern Shandong Peninsula, and the far shore of the East China Sea, while the low Z_{sd} were located in the coastal areas of the Bohai Sea and northern Jiangsu. Concerning long-term variations, Z_{sd} of partial regions (20.84%) exhibited significant increases, particularly in the Bohai Sea and the northern Yellow Sea. Only a few areas (1.14%) showed significant decreases, including Dingzi Bay and Haizhou Bay in the Yellow Sea. In terms of seasonal changes, the highest Z_{sd} occurred in summer, followed by autumn, spring, and winter, and the extend of seasonal variation tends to increase with greater offshore distance. Furthermore, there is a spatial differentiation in the correlations between Z_{sd} and the annual runoff of rivers. The positive correlations are observed in the north and negative correlations in the south, contrasting with the negative correlations between Z_{sd} and annual sediment transport. The findings of this study provide valuable data that can be used to gain insight into long-term changes in the coastal environment of China, which offers novel insights for us to deeply understand the spatiotemporal changes in seawater Z_{sd}.

Data availability statement

The raw data supporting the conclusions of this article will be made available by the authors, without undue reservation.

Author contributions

SC: Conceptualization, Data curation, Formal analysis, Investigation, Methodology, Resources, Software, Validation, Visualization, Writing – original draft, Writing – review & editing. FX: Conceptualization, Funding acquisition, Investigation, Methodology, Project administration, Resources, Supervision, Validation, Visualization, Writing – review & editing. MC: Methodology, Writing – review & editing, Conceptualization, Formal Analysis. ZW: Methodology, Writing – review & editing, Conceptualization, Data curation. JL: Writing – review & editing, Conceptualization, Data curation. YD: Writing – review & editing, Conceptualization, Supervision.

Funding

The author(s) declare financial support was received for the research, authorship, and/or publication of this article. This study was supported by the Key R & D projects in Hubei Province (NO: 2023BCB104), the Key Laboratory for Environment and Disaster Monitoring and Evaluation of Hubei, the Innovation Academy for Precision Measurement Science and Technology, and Chinese Academy of Sciences.

Acknowledgments

We thank the NASA for providing MODIS data, and we also thank the National Field Science Observation and Research Station of Jiaozhou Bay Marine Ecosystem in Shandong Province and the National Earth System Science Data Center for providing transparency measurement data.

Conflict of interest

The authors declare that the research was conducted in the absence of any commercial or financial relationships that could be construed as a potential conflict of interest.

Generative AI statement

The authors declare that no Generative AI was used in the creation of this manuscript.

Publisher's note

All claims expressed in this article are solely those of the authors and do not necessarily represent those of their affiliated organizations, or those of the publisher, the editors and the reviewers. Any product that may be evaluated in this article, or claim that may be made by its manufacturer, is not guaranteed or endorsed by the publisher.

Supplementary material

The Supplementary Material for this article can be found online at: https://www.frontiersin.org/articles/10.3389/fmars.2024.1503177/full#supplementary-material

References

An, Y. H., Feng, X. L., Liu, J., Saito, Y., Qiu, J. D., Zhang, X., et al. (2023). Development of a Middle-Late Holocene subaqueous clinoform in the northern Jiangsu coastal zone, western South Yellow Sea. *Geomorphology* 439, 108853. doi: 10.1016/j.geomorph.2023.108853

Basset, A., Carlucci, D., Fiocca, A., and Vignes, F. (2001). Water transparency and health of coastal salt marshes: simple enclosure experiments on nutrient dynamics. *Aquat. Conserv. Mar. Freshw. Ecosyst.* 11, 273–279. doi: 10.1002/aqc.455

Burn, D. H., and Elnur, M. A. H. (2002). Detection of hydrologic trends and variability. *J. Hydrol.* 255, 107–122. doi: 10.1016/S0022-1694(01)00514-5

Cael, B. B., Bisson, K., Boss, E., Dutkiewicz, S., and Henson, S. (2023). Global climate-change trends detected in indicators of ocean ecology. *Nature* 619, 551–554. doi: 10.1038/s41586-023-06321-z

Chen, M., Xiao, F., Wang, Z., Feng, Q., Ban, X., Zhou, Y., et al. (2022). An improved QAA-based method for monitoring water clarity of Honghu lake using landsat TM, ETM+ and OLI data. *Remote Sens.* 14 (15), 3798. doi: 10.3390/rs14153798

Dai, Y., Yang, S., Zhao, D., Hu, C., Xu, W., Anderson, D. M., et al. (2023). Coastal phytoplankton blooms expand and intensify in the 21st century. *Nature* 615, 280–284. doi: 10.1038/s41586-023-05760-y

Dai, Z. J., Mei, X. F., Darby, S. E., Lou, Y. Y., and Li, W. H. (2018). Fluvial sediment transfer in the Changjiang (Yangtze) river-estuary depositional system. *J. Hydrol.* 566, 719–734. doi: 10.1016/j.jhydrol.2018.09.019

da Silva, R. M., Santos, C. A. G., Moreira, M., Corte-Real, J., Silva, V. C. L., and Medeiros, I. C. (2015). Rainfall and river flow trends using Mann-Kendall and Sen's slope estimator statistical tests in the Cobres River basin. *Nat. Hazards* 77, 1205–1221. doi: 10.1007/s11069-015-1644-7

Dong, L. X., Guan, W. B., Chen, Q., Li, X. H., Liu, X. H., and Zeng, X. M. (2011). Sediment transport in the Yellow Sea and East China Sea. *Estuar. Coast. Shelf Sci.* 93, 248–258. doi: 10.1016/j.ecss.2011.04.003

Edwards, L. J., Muller, K. E., Wolfinger, R. D., Qaqish, B. F., and Schabenberger, O. (2008). An R2 statistic for fixed effects in the linear mixed model. *Stat. Med.* 27, 6137–6157. doi: 10.1002/sim.3429

Fang, G., Yu, H., Sheng, H., Tang, Y., and Liang, Z. (2021). Comparative analysis of microbial communities between water and sediment in Laoshan Bay marine ranching with varied aquaculture activities. *Mar. pollut. Bull.* 173, 112990. doi: 10.1016/j.marpolbul.2021.112990

Feng, L., Hou, X. J., and Zheng, Y. (2019). Monitoring and understanding the water transparency changes of fifty large lakes on the Yangtze Plain based on long-term MODIS observations. *Remote Sens. Environ.* 221, 675–686. doi: 10.1016/j.rse.2018.12.007

Gao, S. K., Yan, K., Liang, B. G., Shu, R. L., Wang, N., and Zhang, S. (2023). The different ways microplastics from the water column and sediment accumulate in fish in Haizhou Bay. *Sci. Total Env.* 854, 158575. doi: 10.1016/j.scitotenv.2022.158575

Gong, G.-C., Wen, Y.-H., Wang, B.-W., and Liu, G.-J. (2003). Seasonal variation of chlorophyll a concentration, primary production and environmental conditions in the subtropical East China Sea. *Deep Sea Res. Part II Top. Stud. Oceanogr.* 50, 1219–1236. doi: 10.1016/S0967-0645(03)00019-5

Gordon, H. R., and Morel, A. Y. (1983). "In — Water Algorithms," in *Remote Assessment of Ocean Color for Interpretation of Satellite Visible Imagery: A Review*. Eds. H. R. Gordon and A. Y. Morel (Springer US, New York, NY), 24–67.

Guo, J., Nie, Y., Sun, B., and Lv, X. (2022). Remote sensing of transparency in the China seas from the ESA-OC-CCI data. *Estuar. Coast. Shelf Sci.* 264, 107693. doi: 10.1016/j.ecss.2021.107693

Guo, J., Pan, H., Cao, R., Wang, J., and Lv, X. (2023a). Multiple timescale variations in water transparency in the eastern China seas over the period 1997–2019. *J. Geophys. Res. Oceans* 128 (4), e2022JC019170. doi: 10.1029/2022jc019170

Guo, J. T., Pan, H. D., Cao, R. C., Wang, J. F., and Lv, X. Q. (2023b). Multiple timescale variations in water transparency in the eastern China seas over the period 1997-2019. *J. Geophys. Res.-Oceans* 128, e2022JC019170. doi: 10.1029/2022JC019170

Guo, J., Zhao, Z., Cao, R., and Lv, X. (2023c). Regional to global assessments of ocean transparency dynamics from 1997 to 2019. *Prog. Oceanogr.* 219, 103165. doi: 10.1016/j.pocean.2023.103165

Harvey, E. T., Walve, J., Andersson, A., Karlson, B., and Kratzer, S. (2019). The effect of optical properties on secchi depth and implications for eutrophication management. *Front. Mar. Sci.* 5. doi: 10.3389/fmars.2018.00496

He, X., Pan, D., and Mao, Z. (2004). *Water-transparency (Secchi Depth) monitoring in the China Sea with the SeaWiFS satellite sensor* (SPIE), 5568. doi: 10.1117/12.564605

Hoellein, T. J., Shogren, A. J., Tank, J. L., Risteca, P., and Kelly, J. J. (2019). Microplastic deposition velocity in streams follows patterns for naturally occurring allochthonous particles. *Sci. Rep.* 9, 3740. doi: 10.1038/s41598-019-40126-3

Hori, K., Saito, Y., Zhao, Q. H., and Wang, P. X. (2002). Architecture and evolution of the tide-dominated Changjiang (Yangtze) River delta, China. *Sediment. Geol.* 146, 249–264. doi: 10.1016/S0037-0738(01)00122-1

Idris, M. S., Siang, H. L., Amin, R. M., and Sidik, M. J. (2022). Two-decade dynamics of MODIS-derived Secchi depth in Peninsula Malaysia waters. *J. Mar. Syst.* 236, 103799. doi: 10.1016/j.jmarsys.2022.103799

Jia, T., Zhang, Y., Weng, C., and Dong, R. (2022). Improving remote sensing retrieval of global ocean transparency with optical water classification. *Ecol. Indic.* 143, 109359. doi: 10.1016/j.ecolind.2022.109359

Jiang, D. L., Matsushita, B., Setiawan, F., and Vundo, A. (2019). An improved algorithm for estimating the Secchi disk depth from remote sensing data based on the new underwater visibility theory. *ISPRS J. Photogramm. Remote Sens.* 152, 13–23. doi: 10.1016/j.isprsjprs.2019.04.002

Lee, Z., Shang, S., Hu, C., Du, K., Weidemann, A., Hou, W., et al. (2015). Secchi disk depth: A new theory and mechanistic model for underwater visibility. *Remote Sens. Environ.* 169, 139–149. doi: 10.1016/j.rse.2015.08.002

Lee, Z., Shang, S., Qi, L., Yan, J., and Lin, G. (2016). A semi-analytical scheme to estimate Secchi-disk depth from Landsat-8 measurements. *Remote Sens. Environ.* 177, 101–106. doi: 10.1016/j.rse.2016.02.033

Lewis, M. R., Kuring, N., and Yentsch, C. (1988). Global patterns of ocean transparency - implications for the new production of the open ocean. *J. Geophys. Res.-Oceans* 93, 6847. doi: 10.1029/JC093iC06p06847

Li, P., Chen, S., Ke, Y., Ji, H., Li, P., and Fan, Y. (2022). Spatiotemporal dynamics of suspended particulate matter in the Bohai Sea, China over the past decade from the space perspective. *Sci. Total Environ.* 851, 158210. doi: 10.1016/j.scitotenv.2022.158210

Li, S., Liang, W., Fu, B., Lü, Y., Fu, S., Wang, S., et al. (2016). Vegetation changes in recent large-scale ecological restoration projects and subsequent impact on water resources in China's Loess Plateau. *Sci. Total Environ.* 569–570, 1032–1039. doi: 10.1016/j.scitotenv.2016.06.141

Liang, L., Chen, M., Luo, X., and Xian, Y. (2021). Changes pattern in the population and economic gravity centers since the Reform and Opening up in China: The widening gaps between the South and North. *J. Clean. Prod.* 310, 127379. doi: 10.1016/j.jclepro.2021.127379

Liang, B. G., Gao, S. K., Wang, Z. Y., Shu, R. L., Wang, N., Tan, W. J., et al. (2023). Spatial distribution characteristics of microplastics in the seawater column and sediments of the artificial reef area and adjacent water in Haizhou Bay. *Sci. Total Env.* 900, 166236. doi: 10.1016/j.scitotenv.2023.166236

Liu, D., Keesing, J. K., Xing, Q., and Shi, P. (2009). World's largest macroalgal bloom caused by expansion of seaweed aquaculture in China. *Mar. pollut. Bull.* 58, 888–895. doi: 10.1016/j.marpolbul.2009.01.013

Liu, Y., Li, J., Xiao, C., Zhang, F., Wang, S., Yin, Z., et al. (2022). A classification-based, semianalytical approach for estimating water clarity from a hyperspectral sensor onboard the ZY1-02D satellite. *IEEE Trans. Geosci. Remote Sens.* 60, 1–14. doi: 10.1109/TGRS.2022.3161651

Mao, Y., Wang, S. Q., Qiu, Z. F., Sun, D. Y., and Bilal, M. (2018). Variations of transparency derived from GOCI in the Bohai Sea and the Yellow Sea. *Opt Express* 26, 12191–12209. doi: 10.1364/Oe.26.012191

Megard, R. O., and Berman, T. (1989). Effects of algae on the secchi transparency of the Southeastern Mediterranean-sea. *Limnol. Oceanogr.* 34, 1640–1655. doi: 10.4319/lo.1989.34.8.1640

Melo, C. E., Lima, J. D., and da Silva, E. F. (2009). Relationships between water transparency and abundance of Cynodontidae species in the Bananal floodplain, Mato Grosso, Brazil. *Neotrop. Ichthyol.* 7, 251–256. doi: 10.1590/S1679-62252009000200017

Milliman, J. D., and Meade, R. H. (1983). World-wide delivery of river sediment to the oceans. *J. Geol.* 91, 1–21. doi: 10.1086/628741

Molner, J. V., Soria, J. M., Pérez-González, R., and Sòria-Perpinyà, X. (2023). Estimating water transparency using sentinel-2 images in a shallow hypertrophic lagoon (The Albufera of Valencia, Spain). *Water* 15 (20), 3669. doi: 10.3390/w15203669

Msusa, A. D., Jiang, D. L., and Matsushita, B. (2022). A semianalytical algorithm for estimating water transparency in different optical water types from MERIS data. *Remote Sens.* 14, 868. doi: 10.3390/rs14040868

Pan, J., Pan, J.-F., and Wang, M. (2014). Trace elements distribution and ecological risk assessment of seawater and sediments from Dingzi Bay, Shandong Peninsula, North China. *Mar. pollut. Bull.* 89, 427–434. doi: 10.1016/j.marpolbul.2014.10.022

Qing, S., Cui, T. W., Lai, Q., Bao, Y. H., Diao, R. X., Yue, Y. L., et al. (2021). Improving remote sensing retrieval of water clarity in complex coastal and inland waters with modified absorption estimation and optical water classification using Sentinel-2 MSI. *Int. J. Appl. Earth Obs. Geoinform.* 102, 102377. doi: 10.1016/j.jag.2021.102377

Qiu, R. T., Wang, S. L., Shi, J. K., Shen, W., Zhang, W. Z., Zhang, F. F., et al. (2023). Sentinel-2 MSI observations of water clarity in Inland waters across Hainan island and implications for SDG 6.3.2 evaluation. *Remote Sens.* 15, 1600. doi: 10.3390/rs15061600

Rao, W. B., Mao, C. P., Wang, Y. G., Huang, H. M., and Ji, J. F. (2017). Using Nd-Sr isotopes and rare earth elements to study sediment provenance of the modern radial sand ridges in the Southwestern Yellow Sea. *Appl. Geochem.* 81, 23–35. doi: 10.1016/j.apgeochem.2017.03.011

Shang, S., Dong, Q., Lee, Z., Li, Y., Xie, Y., and Behrenfeld, M. (2011). MODIS observed phytoplankton dynamics in the Taiwan Strait: an absorption-based analysis. *Biogeosciences* 8, 841–850. doi: 10.5194/bg-8-841-2011

Shang, S. L., Lee, Z., Shi, L. H., Lin, G., Wei, G. M., and Li, X. D. (2016). Changes in water clarity of the Bohai Sea: Observations from MODIS. *Remote Sens. Environ.* 186, 22–31. doi: 10.1016/j.rse.2016.08.020

Shao, T., Zheng, H., Song, K., Zhao, Y., and Zhang, B. (2017). Influence of environmental factors on absorption characteristics of suspended particulate matter and CDOM in Liaohe River watershed, northeast China. *Environ. Sci. pollut. Res.* 24, 19322–19337. doi: 10.1007/s11356-017-9480-9

Shi, Y., and Liu, D. (2018). Excessive urbanization and rejuvenation in the metropolitan city center in Shanghai, China. *J. Urban Plan. Dev.* 144, 05018020. doi: 10.1061/(ASCE)UP.1943-5444.0000486

Shi, W., and Wang, M. H. (2012). Satellite views of the Bohai sea, yellow sea, and East China sea. *Prog. Oceanogr.* 104, 30–45. doi: 10.1016/j.pocean.2012.05.001

Su, M., Yao, P., Wang, Z. B., Zhang, C. K., and Stive, M. J. F. (2017). Exploratory morphodynamic modeling of the evolution of the Jiangsu coast, China, since 1855: Contributions of old Yellow River-derived sediment. *Mar. Geol.* 390, 306–320. doi: 10.1016/j.margeo.2016.10.013

Subash, N., Singh, S. S., and Priya, N. (2011). Variability of rainfall and effective onset and length of the monsoon season over a sub-humid climatic environment. *Atmos. Res.* 99, 479–487. doi: 10.1016/j.atmosres.2010.11.020

Wang, S., Fu, B., Piao, S., Lü, Y., Ciais, P., Feng, X., et al. (2016). Reduced sediment transport in the Yellow River due to anthropogenic changes. *Nat. Geosci.* 9, 38–41. doi: 10.1038/ngeo2602

Wang, C., Li, E., Zhang, L., Wei, H., Zhang, L., and Wang, Z. (2023a). Long-term succession characteristics and driving factors of zooplankton communities in a typical subtropical shallow lake, central China. *Environ. Sci. pollut. Res.* 30, 49435–49449. doi: 10.1007/s11356-023-25782-3

Wang, C., Mao, Y., Zhang, L., Wei, H., and Wang, Z. (2024). Insight into environmental adaptability of antibiotic resistome from surface water to deep sediments in anthropogenic lakes by metagenomics. *Water Res.* 256, 121583. doi: 10.1016/j.watres.2024.121583

Wang, Q., Xu, H., Yin, J., Du, S., Liu, C., and Li, J. (2023b). Significance of the great protection of the Yangtze River: Riverine input contributes primarily to the presence of PAHs and HMs in its estuary and the adjacent sea. *Mar. pollut. Bull.* 186, 114366. doi: 10.1016/j.marpolbul.2022.114366

Wu, S. L., Tao, S. Q., Ye, X., Wang, A. J., Liu, Z. T., Ran, C., et al. (2023). Characteristics of sedimentary organic matter in tidal estuaries: A case study from the Minjiang river estuary. *Water* 15, 1682. doi: 10.3390/w15091682

Xiang, J., Cui, T., Qing, S., Liu, R., Chen, Y., Mu, B., et al. (2023). Remote sensing retrieval of water clarity in clear oceanic to extremely turbid coastal waters from multiple spaceborne sensors. *IEEE Trans. Geosci. Remote Sens.* 61, 1–18. doi: 10.1109/TGRS.2023.3318590

Yamaguchi, H., Kim, H.-C., Son, Y. B., Kim, S. W., Okamura, K., Kiyomoto, Y., et al. (2012). Seasonal and summer interannual variations of SeaWiFS chlorophyll a in the Yellow Sea and East China Sea. *Prog. Oceanogr.* 105, 22–29. doi: 10.1016/j.pocean.2012.04.004

Yin, Z., Li, J., Liu, Y., Xie, Y., Zhang, F., Wang, S., et al. (2021). Water clarity changes in Lake Taihu over 36 years based on Landsat TM and OLI observations. *Int. J. Appl. Earth Obs. Geoinform.* 102, 102457. doi: 10.1016/j.jag.2021.102457

Yu, X., Lee, Z., Shen, F., Wang, M., Wei, J., Jiang, L., et al. (2019). An empirical algorithm to seamlessly retrieve the concentration of suspended particulate matter from water color across ocean to turbid river mouths. *Remote Sens. Environ.* 235, 111491. doi: 10.1016/j.rse.2019.111491

Zhan, J., Zhang, D. J., Zhang, G. Y., Wang, C. X., and Zhou, G. Q. (2020). Estimation of optical properties using qaa-v6 model based on modis data. *Int. Arch. Photogr. Remote Sens Spat. Inf Sci.* 42, 937–940. doi: 10.5194/isprs-archives-XLII-3-W10-937-2020

Zhan, J., Zhang, D., Zhou, G., Zhang, G., Cao, L., and Guo, Q. (2021). MODIS-based research on secchi disk depth using an improved semianalytical algorithm in the yellow sea. *IEEE J. Sel. Top. Appl. Earth Obs. Remote Sens.* 14, 5964–5972. doi: 10.1109/JSTARS.2021.3085556

Zhang, X. B., Bi, S. P., Zhang, Y., Yang, Y., Liu, S. S., Kong, X. H., et al. (2016). Provenance analysis of surface sediments in the Holocene mud area of the southern coastal waters off Shandong Peninsula, China. *Acta Oceanol. Sin.* 35, 124–133. doi: 10.1007/s13131-016-0852-7

Zhang, D., Jia, G., Chen, L., Jin, H., Wang, Z., Feng, W., et al. (2022). Seasonal succession and spatial heterogeneity of the nekton community associated with environmental factors in Hangzhou Bay, China. *Reg. Stud. Mar. Sci.* 49, 102108. doi: 10.1016/j.rsma.2021.102108

Zhao, G., Jiang, W., Wang, T., Chen, S., and Bian, C. (2022). Decadal variation and regulation mechanisms of the suspended sediment concentration in the Bohai sea, China. *J. Geophys. Res. Oceans* 127, e2021JC017699. doi: 10.1029/2021JC017699

Zhao, L., Song, C., Fang, C., Xu, Y., Xin, Z., Liu, Z., et al. (2023). Spatiotemporal variation of long-term surface and vertical suspended particulate matter in the Liaohe estuary, China. *Ecol. Indic.* 151, 110288. doi: 10.1016/j.ecolind.2023.110288

Zheng, X., Fu, Z., Xi, Y., Mu, J., and Li, Y. (2014). Grey relationship analysis for the environmental factors affecting the Noctiluca scintillans density in Qinhuangdao coastal area. *Prog. Fish. Sci.* 35, 8–15.

Zhou, Y., Yu, D., Yang, Q., Pan, S., Gai, Y., Cheng, W., et al. (2021). Variations of water transparency and impact factors in the bohai and yellow seas from satellite observations. *Remote Sens.* 13 (3), 514. doi: 10.3390/rs13030514